Article:
Lashgari, M orcid.org/0000-0002-5307-3495, Shahmoradi, M, Rabbani, H et al. (1 more author) (2018) Missing Surface Estimation Based on Modified Tikhonov Regularization: Application for Destructed Dental Tissue. IEEE Transactions on Image Processing, 27 (5). pp. 2433-2446. ISSN 1057-7149

https://doi.org/10.1109/TIP.2018.2800289

Missing Surface Estimation Based on Modified Tikhonov Regularization: Application for Destructed Dental Tissue

Mojtaba Lashgari, Mahdi Shahmoradi, Hossein Rabbani*, Senior Member, IEEE, Michael Swain

Abstract— Estimation of missing digital information is mostly addressed by one or two-dimensional signal processing methods; however, this problem can emerge in multi-dimensional data including 3D images. Examples of 3D images dealing with missing edge information are often found using dental micro-CT, where the natural contours of dental enamel and dentine are partially dissolved or lost by caries. In this paper, we present a novel sequential approach to estimate the missing surface of an object. First, an initial correct contour is determined interactively or automatically, for the starting slice. This contour information defines the local search area and provides the overall estimation pattern for the edge candidates in the next slice. The search for edge candidates in the next slice is performed in the perpendicular direction to the obtained initial edge in order to find and label the corrupted edge candidates. Subsequently, the location information of both initial and nominated edge candidates are transformed and segregated into two independent signals (X-coordinates and Y-coordinates) and the problem is changed into error concealment. In the next step, the missing samples of these signals are estimated using a modified Tikhonov regularization model with two new terms. One term contributes in the denoising of the corrupted signal by defining an estimation model for a group of mildly destructed samples, and the other term contributes in the estimation of the missing samples with the highest similarity to the samples of the obtained signals from the previous slice. Finally, the reconstructed signals are transformed inversely to edge pixel representation. The estimated edges in each slice are considered as initial edge information for the next slice and this procedure is repeated slice by slice until the entire contour of the destructed surface is estimated. The visual results as well as quantitative results (using both contour-based and area-based metrics) for seven image datasets of tooth samples with considerable destruction of the dentin-enamel junction (DEJ) demonstrates that the proposed method can accurately interpolate the shape and the position of the missing surfaces in computed tomography images in both two and three dimensions (e.g. 14.87±3.87 µm of mean distance (MD) error for the proposed method versus 7.33±0.27 µm of MD error between human experts and 1.25±~0 % error rate (ER) of the proposed method versus 0.64±~0 % of ER between human experts (~1% difference)).

Keywords: missing contour estimation, Tikhonov regularization, dental micro-CT, error concealment

I. INTRODUCTION

ESTIMATION and restoration of the contour and morphology of the lost structures in images of damaged and destroyed tissues are critical tasks in biomedical fields. Estimated structural information of the deteriorated tissue in its pre-damaged state can be employed for a variety of applications, such as automatic machine-based disease diagnosis and 3D tissue restoration [1, 2]. A recent emerging field in biomedical engineering is the application of 3D printing and computer-assisted design and manufacturing (CAD/CAM) technologies for reconstructing hard tissues, making scaffolds, organ 3D models and analogs from CAD data (Figure 1). 3D images from non-destructive imaging modules such as computed tomography (CT) and Magnetic Resonance Imaging (MRI) are the main sources of information for CAD/CAM based tissue engineering.

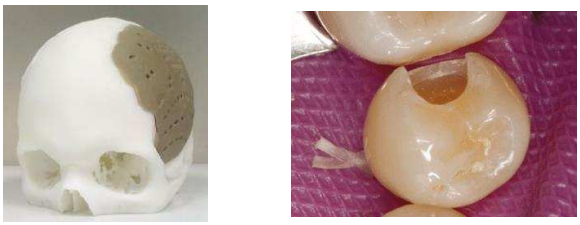

a b

Fig.1. a) 3D printed skull cap for the repair of cranial damage. b) A proximal surface dental cavity in need of a restoration.

Biological entities such as tooth, bone, vessels and skin usually have multilayer structures which are composed of several components with different biological, structural and functional specifications. Therefore, modeling, design and fabrication of tissue constructs, and restorations entail consideration of these layers and reconstruction of the interfaces between various tissue components. A common example of these cases is found using dental 3D images, where the interface between dental enamel and dentine is partially dissolved or lost by caries. Ideal restoration of the lost dental tissue requires the replacement of dentinal and enamel components using materials with matching mechanical and structural properties. Considering the large number of images in each CT/MRI database, the reconstruction of the destructed or damaged anatomical contours in stacks of CT/MRI images using accurate machine-based methods is a valuable objective for both clinical and engineering applications. In addition, since the performance of 3D segmentation methods generally relies on the existing information of the imaged object, many of the existing 3D image segmentation approaches (e.g. level-sets, freely deformable models, statistical shape models) are not applicable for image stacks with considerable absence of the surfaces and edges of the captured object.

Various methods such as edge linking and binary image inpainting [3-9] have been used to address this problem in 2D space. However, these methods have not been able to provide satisfactory restoration results in all 2D cases and they have limited efficacy for 3D images. For example, morphological-based edge linking methods distort the true edges and fail in estimating the contours with large gaps present [10, 11]. Non-morphological-based edge linking methods, which depend on image intensity [12, 13], often fail in estimating the correct

M. Lashgari and H. Rabbani are with School of Advanced Technologies in Medicine and Medical Image & Signal Processing Research Center, Isfahan University of Medical Sciences, Isfahan, Iran, Postal code: 81746-73461, Phone: 98 (31) 37925262, Fax: 98 (31) 37923927, Email: rabbani.h@ieee.org.

M. Shahmoradi and M. Swain are with dental biomaterials and bioengineering department, The University of Sydney, Australia.

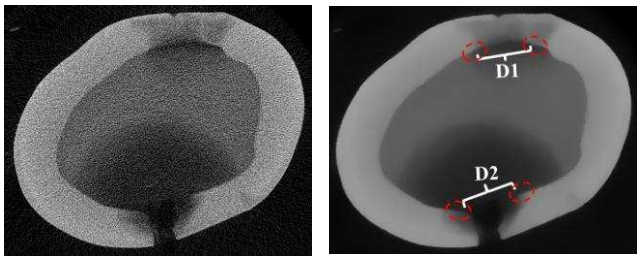

a b

Fig. 2. Horizontal microCT slice of a tooth sample with DEJ and external surface destruction. a) Noisy image, b) Denoised image by total variation.

contour of destructed objects that lack sufficient intensity information. On the other hand, non-morphological-based edge linking methods which are intensity independent, are inefficient in estimating curved contours as they usually create a straight line to connect the edges of the missing structure [14-19]. In the case of binary image inpainting methods, the main deficiency of these methods is their infirmity to restore binary images with one-pixel width (OPW). This infirmity traces back to the inherent need of PDE-based methods to boundary conditions, which are not satisfactorily provided by OPW objects. To overcome this problem, thin binary objects are thickened using morphological operators before interpolation, which leads to the distortion of the original shape of the object [3].

To the knowledge of the authors, few 3D image inpainting methods have been proposed for the estimation of the shape and contour of a missing surface in 3D images. A 3D inpainting method based on a new shape multiscale representation (MSR) was developed by Dong et al. [20] in order to estimate the boundary of the corrupted arteries and to quantify the degree of arteriosclerosis and vessel occlusion. The weakness of this method is the approximated reconstruction, instead of exact reconstruction, for the inverse transformation [21]. In another study, Schmieder [22] introduced a mean/Gaussian elastica model for estimation of the broken cell paths in 3D fluorescent microscopy images. Although the developed method has the ability to recover shapes across large in-paint domains, the proposed model is difficult to solve numerically and its equation evolves very slowly.

In view of the increasing application of machine-based contour estimation methods for biomedical and engineering purposes and considering the limitations of the above-mentioned solutions, we propose a sequential approach for the estimation and reconstruction of the pre-existing contour of a damaged or missing surface in 3D images. The novelty of the proposed work is that in this method the information from a 3D image is evolved into 1D signals, providing the opportunity to address a 3D image processing issue as a 1D signal processing problem. Subsequently, the application of an error concealment method [23] based on a modified Tikhonov regularization model (TRM) with two new regularization terms leads to an accurate and convenient estimation of the corrupted samples of the missing surface in 3D. In addition, since a consecutive approach is employed in this method, there is no need for simultaneous processing of all images of the dataset. Therefore, the computational cost and the required time for the implementation of the method are considerably lowered.

The suggested method may find various applications in biomedical and engineering fields. However, as a practical example, we have applied our method to seven image datasets of tooth samples with considerable destruction of the dentin-enamel junction (DEJ) interface. In this case, the goal was to estimate and reconstruct the destructed contour of the interfacial surface between dentin and enamel (D1 and D2 in Figure 2).

Details of the data preparation step, including the specimen collection, image acquisition and denoising of micro-CT images, are provided in Section II. The proposed contour estimation method is explained in Section III. Experimental results from applying the proposed method to dental micro-CT image datasets are presented in Section IV. Finally, a discussion along with a conclusion and direction of further work are presented in Section V.

II. Data Preparation

Extracted human teeth with significant destruction of enamel and dentin were collected from the Oral Surgery Department at Sydney Dental Hospital, University of Sydney, according to protocols approved by Sydney Local Health District Ethics Review Committee, Protocol No X12-0065 & HREC/12/RPAH/106.

Imaging was performed using a high-resolution micro-CT system (Skyscan, Aartselaar, Belgium) with continuous mode exposures at 0.5 s intervals, a binning value of 2, an accelerating voltage of 60kV and a current of 120 μA. Resultant reconstructed images had an isotropic pixel resolution of 8.9 μm and a dynamic range of 16 bits with an image matrix of 2000×2000 pixels. The denoising of the images was performed using the total variation method [24, 25]. Figure 2 shows the original noisy as well as the result of the denoising process on a nominated dental micro-CT image.

III. Method

The proposed estimation method is conceptually based on a 1D signal processing technique called error concealment [26] in which the missing samples of a signal are retrieved from available uncorrupted samples in order to minimize the deterioration of the signal.

Figures 3.a and 3.b depict a corrupted signal and the corresponding restored signal after error concealment. By considering this corrupted signal as a corrupted OPW binary image, it would be possible to restore the corrupted region of this OPW binary image in the same way that a corrupted signal is restored. Therefore, by transforming the binary image of the dentin-enamel junction (DEJ) interface into 1D signals, which represent X- and Y- coordinates of the location of the pixels, we can solve the problem of restoring the corrupted interface as a 1D signal processing problem.

Since X- and Y- coordinates of the location of the pixels are independent of each other, we can segregate X- and Y-coordinates of each pixel into two separate signals. If we indicate the X- and Y- coordinates of edge pixels by $(\boldsymbol{x^i}, \boldsymbol{y^i})$, where $\mathbf{1} \leq \boldsymbol{i} \leq \boldsymbol{n}$, and $\boldsymbol{n}$ is the number of edge pixels, the transformed 1D signals, $\boldsymbol{C_x}$: $\{\mathbf{1}, \dots, \boldsymbol{n}\} \rightarrow \mathbb{N}$ and $\boldsymbol{C_y}$: $\{\mathbf{1}, \dots, \boldsymbol{n}\} \rightarrow \mathbb{N}$, are defined as $\boldsymbol{C_x^i} = \boldsymbol{x^i}$ and $\boldsymbol{C_y^i} = \boldsymbol{y^i}$ respectively.

As an example, we consider the transformation of the white boundary (that surrounds the central black pixel in Figure 4.a)

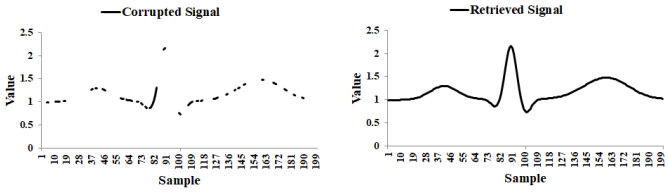

a b

Fig. 3. a) Corrupted signal, b) Retrieved signal after error concealment [26].

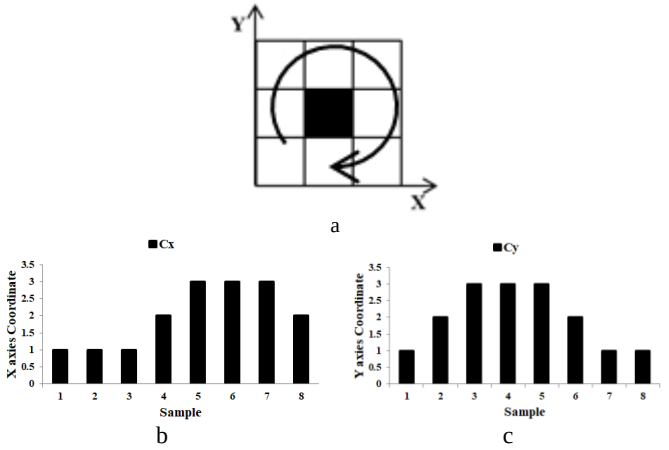

a b c

Fig. 4 Location information of the edge (white boundary that surrounds the central black pixel) is represented as two 1D signals. a) edge pixels, b) C_x, c) C_y

into two 1D signals, where C_x (Figure 4.b) is decomposed as

$$\{1,2,3,4,5,6,7,8\} \rightarrow \{1,1,1,2,3,3,3,2\}$$

and C_y (Figure 4.c) as

$$\{1,2,3,4,5,6,7,8\} \rightarrow \{1,2,3,3,3,2,1,1\}$$

Figure 5.a shows the initial edge information of the sound DEJ and Figures 5.b and 5.c depict the resultant C_x and C_y signals respectively.

After transforming the OPW object into two 1D signals, the next step is the retrieval of the corrupted samples of the signals, which correspond to the corrupted part of the OPW binary object, using error concealment techniques.

As shown in Figure 5.a, the contour of the sound DEJ has a smooth and gradual curve. Therefore, the resultant transformed 1D signals of the sound DEJ (Figures 5.b and 5.c) and the final estimated signals of the destructed DEJ should possess a gradual contour with a smooth function as well. Considering these features of the original and corrupted signals, we employ the TRM as the error concealment technique [27].

TRM solves the problem of estimating signal e by minimizing the following objective function

$$\min_{e} \quad \|c - e\|_2^2 + \lambda \|D'' e\|_2^2 \qquad (1)$$

where c is the observed signal, λ is the regularization parameter and D'' is the second-difference matrix [27]. If the original TRM is applied to the transformed signals of an image slice, the values of the missing samples will be estimated only by employing the information of non-corrupted samples of the same slice and without incorporating the information from the adjacent slices. This will result in non-cohesive and disharmonious reconstruction of the 3D contour. This limitation of the original TRM for the estimation of the corrupted DEJ contour will be discussed in more detail in Section V. To overcome this problem, we add two new terms to Eq. (1), to incorporate the information of the signals from the previous slice in our estimation. The details of these added terms are provided in subsection III.C of the proposed method. After retrieving the missing samples of both C_x and C_y signals, the values of the signals are inversely transformed to pixel presentation to be placed in the image plane. An overview of the block diagram of the proposed method is shown in Figure 6. The block diagram is composed of four main subsections. Each subsection will be described individually in the following paragraphs:

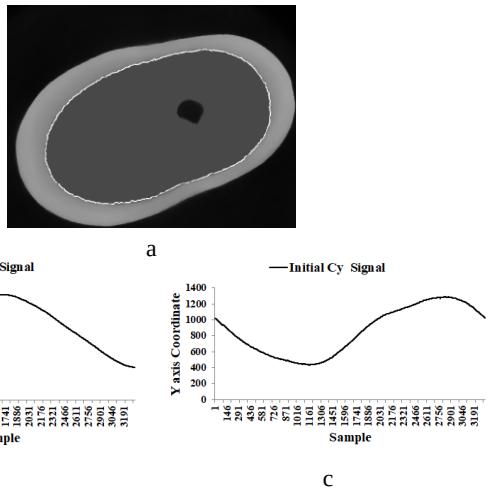

a b c

Fig. 5. a) Initial edge information b) X axis coordinate (C_x) c) Y axis coordinate (C_y).

A. Initializing the edge information

First, the required variables are initialized whereby

r_{in}: *interal search radius*
r_{ex}: *external search radius*
n = *length of initial edge*
$T_{dent.}$: *minimum intensity of sound dentin*
$T_{enam.}$: *minimum intensity of sound enamel*
$T_{grad.}$: *minimum gradient value*

Second, the correct location of the DEJ in the starting slice is extracted from a single 2D image with a non-corrupted DEJ contour or is determined by the user in one of the slices with destructed DEJ. This information will be utilized to determine the initial local search area for finding the position of the edge candidates in the next slices (Figure 7), and also will provide a general pattern for estimating the missing samples in the resultant 1D signals of the destructed DEJ.

B. Forming the corrupted signals

In this step, the positions of possible edge candidates in the next slice are determined by searching within the initial edge area, which was obtained from the previous slice (Figure 7). The position of these edge candidates forms the corrupted signals of the current slice as explained earlier.

Before further explaining this approach, we should clarify that the subscript k indicates the number of slice and the superscript indicates the position of an array within a vector or a matrix. In addition, we define I as a function that returns the gray value for each pixel position. Also, we define the discrete differential operator as $\frac{d}{dj} f = f(j+1) - f(j)$.

Let the corresponding location of the pixels of the perpendicular line to the i^{th} pixel of the initial edge of the $k\text{-}1^{th}$ slice, i.e. (x_{k-1}^i, y_{k-1}^i), is represented by

$$P_{\perp,k}^{i,j} = \{(x_k^j, y_k^j) ; \forall j \in [1, r_{ex} + r_{in}]\}. \qquad (2)$$

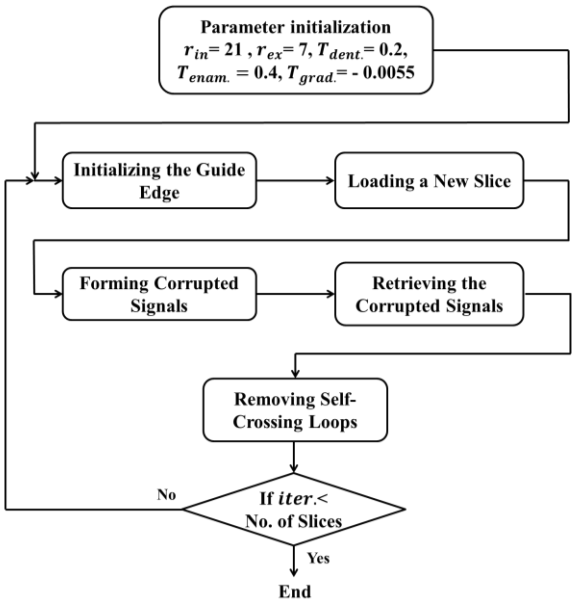

Fig. 6. Block diagram of the proposed algorithm for estimation of a missing surface in 3D.

First, for the i^{th} pixel of the initial edge in the k^{th} slice, $P^{i,j}_{\perp,k}$ is extracted. Second, as the regions around the destructed DEJ have significant mineral density loss, the intensity of these regions in both enamel and dentin areas are less than their sound counterparts. Accordingly, if the average intensities of the related pixels in the external and internal parts of $P^{i,j}_{\perp,k}$ are less than $T_{enam.}$ and $T_{dent.}$ respectively, i.e.

$$\sum_{j=1}^{r_{ex}} I(x^j_k, y^j_k)/r_{ex} \le T_{enam.} \quad (3)$$

and

$$\sum_{j=1+r_{ex}}^{r_{ex}+r_{in}} I(x^j_k, y^j_k)/r_{in} \le T_{dent.} \quad (4)$$

then $P^{i,j}_{\perp,k}$ is considered to be located in the destructed region and therefore the value of the related corrupted samples in both $C^{\,i}_{x_k}$ and $C^{\,i}_{y_k}$ will be assigned u, as an unknown value (extracted pixels of $P^{150,j}_{\perp,k}$ in Figure 7, right bottom corner). Otherwise, the location of the most dominant gradient in the perpendicular line, i.e.

$$j^* = argmin \frac{d}{dj} I(P^{i,j}_{\perp,k}) \quad (5)$$

in which

$$\frac{d}{dj} I(x^j_k, y^j_k)|_{j=j^*} \le T_{grad.} \quad (6)$$

will be allocated to the value of the samples in $C^{\,i}_{x_k}$ and $C^{\,i}_{y_k}$ (extracted pixels of $P^{1,j}_{\perp,k}$, shown in the left side of Figure 7). In the rare case of low intensity variation, where the intensity gradient across the perpendicular line does not reveal any sharp edges which satisfy Eq. (6) the values of the related samples are considered as u too (extracted pixels of $P^{50,j}_{\perp,k}$ in Figure 7, right top corner).

The explained procedure is repeated for all pixels of the initial edge to form C_{y_k} and C_{x_k}. The following algorithm shows the procedure of forming the corrupted signals.

Algorithm for forming the corrupted signals

For $i = 1 : n$
  Extract $(P^{i,j}_{\perp,k})$ on (x^i_{k-1}, y^i_{k-1})
  If $\left(\sum_{j=1}^{r_{ex}} I(x^j_k, y^j_k)/r_{ex} \le T_{enam.}\right) and \left(\sum_{j=1+r_{ex}}^{r_{ex}+r_{in}} I(x^j_k, y^j_k)/r_{in} \le T_{dent.}\right)$
    $C_{y_k}{}^{i} = u$
    $C_{x_k}{}^{i} = u$
  Else if $j^* = argmin\ \frac{d}{dj} P^{i,j}_{\perp,k}\ ;\ \frac{d}{dj} I(x^j_k, y^j_k)|_{j=j^*} \le T_{grad.}$
    $C_{y_k}{}^{i} = y^j_k$
    $C_{x_k}{}^{i} = x^j_k$
  Else
    $C_{y_k}{}^{i} = u$
    $C_{x_k}{}^{i} = u$
  End
End

Figures 8.a and 8.b show the corrupted signals, C_x and C_y, associated with Figure 2.b. Missing samples corresponding to the destructed DEJ regions (D1 and D2 in Figure 2) are also observable in Figure 8.

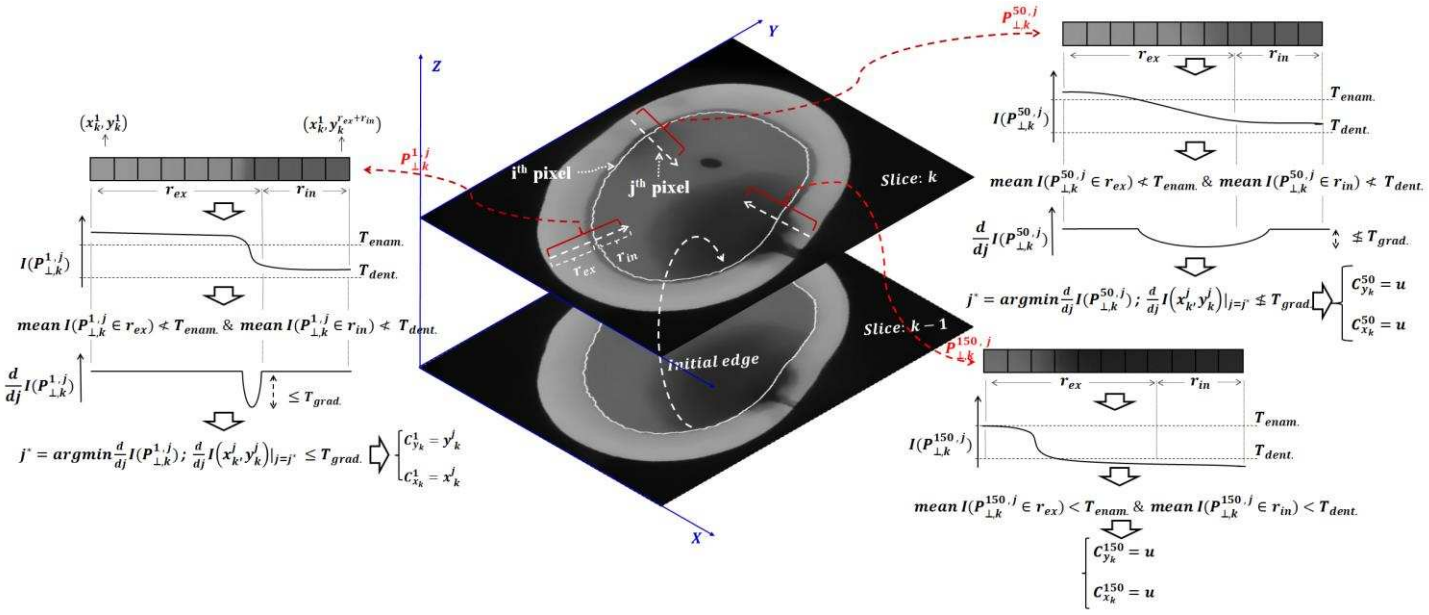

Fig. 7. Schematic of the sequential approach for searching the edge candidates in the current slice (k) by utilization of the determined edge information from the previous slice (k-1).

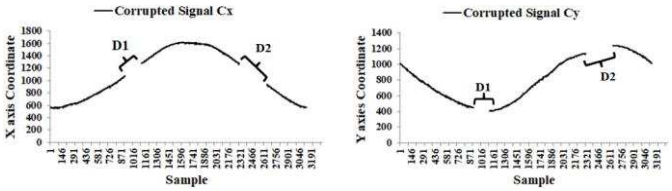

a b

Fig. 8. The resultant signals from the edge candidate searching process. a) X axis coordinate (C_x), b) Y axis coordinate (C_y).

C. Retrieving the corrupted signals

Before formulation of the modified TRM, we introduce some notations. Let c be the corrupted signal of length N, K determines non-corrupted samples of c, where $K < N$ and S indicates the sampling matrix of size $K \times N$. For instance, if the first, second, fifth and sixth samples of a 7-point signal c are known, i.e. $c(0)$, $c(1)$, $c(4)$ and $c(5)$, then S is given by:

$$S = \begin{bmatrix} 1 & 0 & 0 & 0 & 0 & 0 & 0 \\ 0 & 1 & 0 & 0 & 0 & 0 & 0 \\ 0 & 0 & 0 & 0 & 1 & 0 & 0 \\ 0 & 0 & 0 & 0 & 0 & 1 & 0 \end{bmatrix} \quad (7)$$

The matrix S is the identity matrix with rows removed, corresponding to the missing samples. Sc removes three corrupted samples from the signal c,

$$Sc = \begin{bmatrix} 1 & 0 & 0 & 0 & 0 & 0 & 0 \\ 0 & 1 & 0 & 0 & 0 & 0 & 0 \\ 0 & 0 & 0 & 0 & 1 & 0 & 0 \\ 0 & 0 & 0 & 0 & 0 & 1 & 0 \end{bmatrix} \begin{bmatrix} c(0) \\ c(1) \\ c(2) \\ c(3) \\ c(4) \\ c(5) \\ c(6) \end{bmatrix} = \begin{bmatrix} c(0) \\ c(1) \\ c(4) \\ c(5) \end{bmatrix} \quad (8)$$

We define S_s, as the similarity matrix, which consists of the rows of an identity matrix corresponding to the missing samples. Additionally, for each group of missing samples with a minimum number of N_g , N_a adjacent samples are also selected. For instance, for a group of two missing samples ($N_g = 2$) in the corrupted signal of c, if one adjacent sample is selected ($N_a = 1$), S_s would be

$$S_s = \begin{bmatrix} 0 & 1 & 0 & 0 & 0 & 0 & 0 \\ 0 & 0 & 1 & 0 & 0 & 0 & 0 \\ 0 & 0 & 0 & 1 & 0 & 0 & 0 \\ 0 & 0 & 0 & 0 & 1 & 0 & 0 \\ 0 & 0 & 0 & 0 & 0 & 0 & 1 \end{bmatrix} \quad (9)$$

in which the second, third and fifth rows extract corrupted samples of signal c , i.e. $c(2)$, $c(3)$ and $c(6)$. Since $c(2)$ and $c(3)$ form a group of two successive missing samples (N_g), therefore the first and fourth rows of Eq. (9) extract $c(1)$ and $c(4)$ as adjacent samples (N_a), as follows:

$$S_s c = \begin{bmatrix} 0 & 1 & 0 & 0 & 0 & 0 & 0 \\ 0 & 0 & 1 & 0 & 0 & 0 & 0 \\ 0 & 0 & 0 & 1 & 0 & 0 & 0 \\ 0 & 0 & 0 & 0 & 1 & 0 & 0 \\ 0 & 0 & 0 & 0 & 0 & 0 & 1 \end{bmatrix} \begin{bmatrix} c(0) \\ c(1) \\ c(2) \\ c(3) \\ c(4) \\ c(5) \\ c(6) \end{bmatrix} = \begin{bmatrix} c(1) \\ c(2) \\ c(3) \\ c(4) \\ c(6) \end{bmatrix} \quad (10)$$

Also D' and D'' are defined as the first-difference and second-difference matrices respectively as follows:

$$D' = \begin{bmatrix} 1 & -1 & 0 & \cdots & 0 \\ 0 & 1 & -1 & & \\ \vdots & & \ddots & & \vdots \\ 0 & & \cdots & 1 & -1 \end{bmatrix} \quad (11)$$

$$D'' = \begin{bmatrix} 1 & -2 & 1 & 0 & 0 & & & 0 \\ 0 & 1 & -2 & 1 & 0 & \cdots & & \\ 0 & 0 & 1 & -2 & 1 & & & \\ & \vdots & & & & \ddots & & \vdots \\ & 0 & & & & \cdots & 1 & -2 & 1 \end{bmatrix} \quad (12)$$

The formula of the modified TRM is developed by modifying the fidelity term of the objective function, $\|c - e\|_2^2$, and adding two extra terms, called similarity terms, to the original formula as follows:

$$\min_{e} \|\alpha S(c - e)\|_2^2 + \|\beta D'' e\|_2^2 + \|\gamma S_s(e - z)\|_2^2 + \|\zeta S_s D'(e - z)\| \quad (13)$$

where c, e and z are the corrupted, estimated and previous slice signals respectively, and α, β, γ and ζ are diagonal matrices of coefficients that determine the effect of each term of Eq. (13) on the final result.

The first term of the objective function in Eq. (13) i.e. $\|S(c - e)\|_2^2$, preserves the values of the known samples of the corrupted signal, which are selected by the sampler matrix S, for inclusion in the final resultant signals.

The second term $\|\beta D'' e\|_2^2$ has two roles, namely denoising and estimating the corrupted signal simultaneously. Regarding its denoising role, since the directions of the perpendicular lines to a pixel in the digital image plane are limited to 4 directions i.e. $\measuredangle 135$, $\measuredangle 45$, $\measuredangle 90$ and $\measuredangle 180$, the values of some samples in the corrupted C_{x_k} and C_{y_k} signals represent incorrect edge locations and therefore cause the distortion of the signal (Figures 9.a and b). In order to remove this distortion, $\|\beta D'' e\|_2^2$ is applied to denoise the corrupted signals, C_{x_k} and C_{y_k} , shown in Figure 10. Regarding the estimating role of $\|\beta D'' e\|_2^2$, it enforces the estimated samples to approximately follow the curve shape and smooth trend of the known samples of the existing signal. Since the level of required smoothing is different for known and missing samples, the values of the coefficient matrix of β are defined in a way that the value of the coefficients of N_g group of missing samples is different from that of known samples of C_{x_k} and C_{y_k} signals. For example, β for c in Eq. (8), will be as follows, where $c(2)$ and $c(3)$ form a group of two successive missing samples:

$$\begin{bmatrix} b & 0 & 0 & 0 & 0 & 0 & 0 \\ 0 & b & 0 & 0 & 0 & 0 & 0 \\ 0 & 0 & a & 0 & 0 & 0 & 0 \\ 0 & 0 & 0 & a & 0 & 0 & 0 \\ 0 & 0 & 0 & 0 & b & 0 & 0 \\ 0 & 0 & 0 & 0 & 0 & b & 0 \\ 0 & 0 & 0 & 0 & 0 & 0 & b \end{bmatrix} \quad (14)$$

The third term of the objective function i.e. $\|\gamma S_s(e - z)\|_2^2$ contributes, alongside $\|\beta D'' e\|_2^2$, in denoising of the corrupted signal by defining an estimation model for a group of mildly destructed samples. Due to the wide range of intensity loss, from none to total loss in DEJ, some mildly destructed DEJ candidates having a mineral density close to the sound DEJ but not belonging to the true location of DEJ, are also identified inadvertently as sound samples of C_{x_k} and C_{y_k}signals. The sample values obtained from these marginal regions (red dashed circle in Figure 2.b), can impose severe distortion within the C_{x_k} and C_{y_k} signals. To prevent this issue, we modify the value of these marginal samples based on the corresponding samples of the initial signal from the previous slice by adding $\|\gamma S_s(e - z)\|_2^2$ to the objective function. γ localizes the effect of $\|S_s(e - z)\|_2^2$ to N_a marginal samples of C_{x_k} and C_{y_k} signals. For instance, γ for $S_s c$ in Eq. (10) will be as follows, where $c(2)$ and $c(3)$ form a group of two successive missing samples and $c(1)$ and $c(4)$ are adjacent samples:

$$\begin{bmatrix} d & 0 & 0 & 0 & 0 \\ 0 & 0 & 0 & 0 & 0 \\ 0 & 0 & 0 & 0 & 0 \\ 0 & 0 & 0 & d & 0 \\ 0 & 0 & 0 & 0 & 0 \end{bmatrix} \quad (15)$$

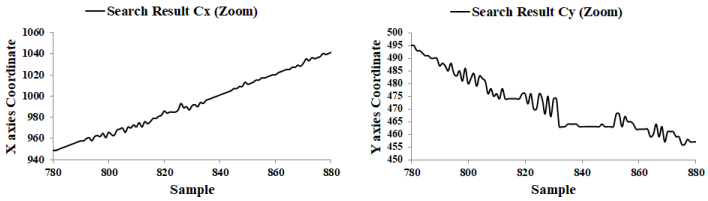

a b

Fig. 9. 100 known samples for a corrupted signal a) X axis coordinate (C_x), b) Y axis coordinate (C_y).

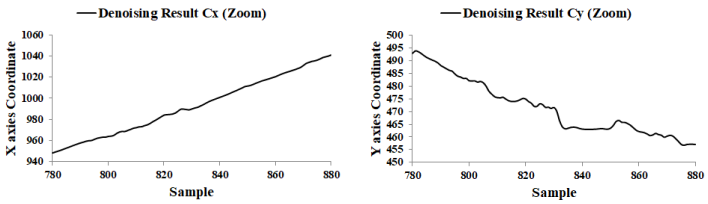

a b

Fig. 10. Denoising result for 100 known samples of a corrupted signal a) X axis coordinate (C_x), b) Y axis coordinate (C_y).

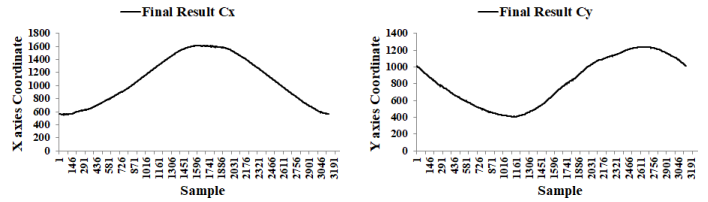

a b

Fig. 11. Results of estimating the missing samples a) X axis coordinate (C_x) b) Y axis coordinate (C_y).

The fourth term, $\|\boldsymbol{\zeta S_s D}'(\boldsymbol{e}-\boldsymbol{z})\|_2^2$ contributes, alongside $\|\boldsymbol{\beta D}''\boldsymbol{e}\|_2^2$, in the estimation of the missing samples with the highest similarity to the samples of the obtained signals from the DEJ of the previous slice. $\boldsymbol{\zeta}$ localizes the effect of $\|\boldsymbol{S_s D}'(\boldsymbol{e}-\boldsymbol{z})\|_2^2$ to the group of missing samples with a minimum of $\boldsymbol{N_g}$ samples. For example, $\boldsymbol{\zeta}$ for $\boldsymbol{S_s c}$ in Eq.(10) will be as follows:

$$\begin{bmatrix} \mathbf{0} & \mathbf{0} & \mathbf{0} & \mathbf{0} & \mathbf{0} \\ \mathbf{0} & \boldsymbol{f} & \mathbf{0} & \mathbf{0} & \mathbf{0} \\ \mathbf{0} & \mathbf{0} & \boldsymbol{f} & \mathbf{0} & \mathbf{0} \\ \mathbf{0} & \mathbf{0} & \mathbf{0} & \mathbf{0} & \mathbf{0} \\ \mathbf{0} & \mathbf{0} & \mathbf{0} & \mathbf{0} & \mathbf{0} \end{bmatrix} \quad (16)$$

therefore, by solving Eq. (13), we achieve the result

$$\boldsymbol{e} = \left(\boldsymbol{S}^T\boldsymbol{\alpha}^T\boldsymbol{\alpha S} + \boldsymbol{S_s}^T\boldsymbol{\gamma}^T\boldsymbol{\gamma S_s} + \boldsymbol{D}'^T\boldsymbol{S_s}^T\boldsymbol{\zeta}^T\boldsymbol{\zeta S_s D}' + \boldsymbol{D}''^T\boldsymbol{\beta}^T\boldsymbol{\beta D}''\right)^{-1} \times \left(\boldsymbol{S}^T\boldsymbol{\alpha}^T\boldsymbol{\alpha Sc} + \left(\boldsymbol{S_s}^T\boldsymbol{\gamma}^T\boldsymbol{\gamma S_s} + \boldsymbol{D}'^T\boldsymbol{S_s}^T\boldsymbol{\zeta}^T\boldsymbol{\zeta S_s D}'\right)\boldsymbol{z}\right) \quad (17)$$

Figure 11 shows the results of estimating the missing samples of the presented signals in Figure 8.

D. Removing the self-crossing loop

In some cases, the located edge candidates may form a self-crossing loop on the restored contour. Figures 12 and 13.a illustrate the formation of a self-crossing loop during the search process. Self-crossing loops do not form very commonly, but they can disturb the entire tracking procedure when they occur. Several approaches [28-31] have addressed this problem. To resolve the likely self-crossing loop problem, we choose the proposed method by Nakhmani [31] as it has straightforward implementation and low running time. Figure 13 shows the result of Nakhmani's method for self-crossing loop removal.

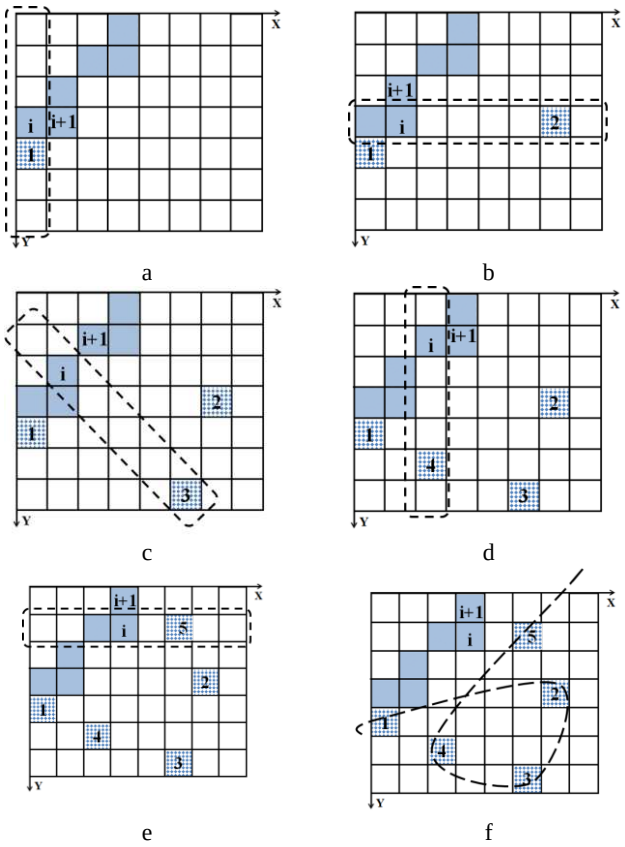

a b c d e f

Fig. 12. Formation of a small self-crossing loop during the search process.

a b

Fig. 13. a) Self-crossing loop b) Removing the self-crossing loop after the application of Nakhmani's method.

After retrieving the corrupted signals and removing possible self-crossing, paired coordinates composed of the matched samples of the two estimated signals ($\boldsymbol{C}_{x_k^i}, \boldsymbol{C}_{y_k^i}$) are used to locate the position of the destructed DEJ in the image plane. As illustrated in the main block diagram in Figure 6, the procedures of Section III.A to III.D, continue slice by slice until all the images of the stack are processed.

IV. Experimental Result

For the visual and quantitative evaluation of the proposed method, we set the coefficients of Eq. (17) in a way that $\boldsymbol{N_g}$ and $\boldsymbol{N_a}$ in $\boldsymbol{S_s}$, include 20 samples each. Moreover, for all samples of each corrupted signal, the diagonal values for $\boldsymbol{\alpha}$ and $\boldsymbol{\beta}$ matrices are set to one except for a group of 20 missing samples ($\boldsymbol{N_g}$) for which the diagonal arrays are 0.9. The values of the coefficient matrix of $\boldsymbol{\gamma}$ for a group of 20 missing samples ($\boldsymbol{N_g}$) are assigned as zero and for a group of 20 adjacent samples ($\boldsymbol{N_a}$) as three. The values of $\boldsymbol{\zeta}$ for a group of 20 missing samples ($\boldsymbol{N_g}$) are assigned as 0.6 and for a group of 20 adjacent samples ($\boldsymbol{N_a}$) as zero.

a b

Fig. 14. 3D visualization of the final results of the estimation of missing surfaces in a nominated dataset. a) A known values of DEJ interface (green color). b) Estimated values of DEJ interface (red color).

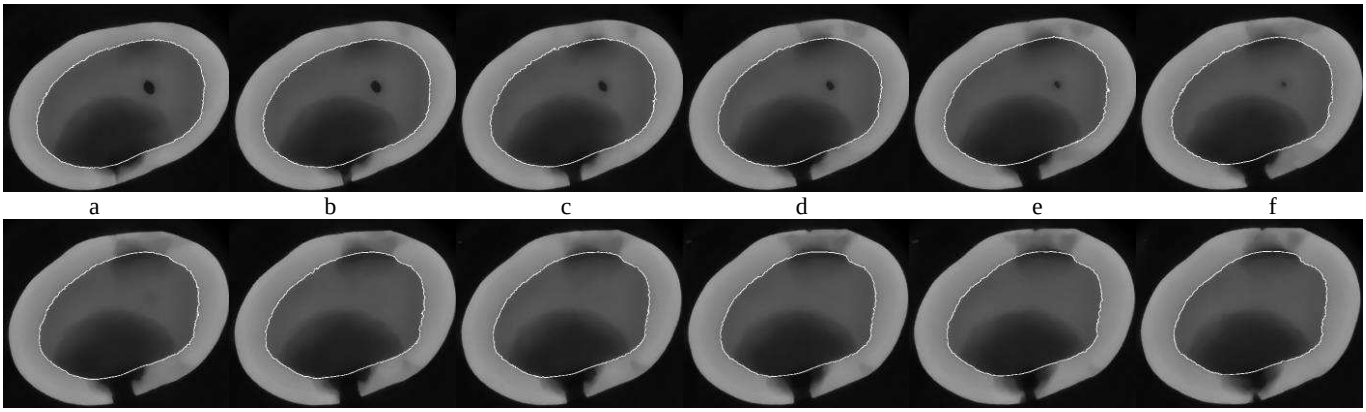

a b c d e f

g h i j k l

Fig. 15. Selected horizontal slices of the final results of the estimation process corresponding to the depicted volume in Figure 12, showing the accurate estimation of the destructed DEJ contour and precise tracking of the DEJ interface in sound areas.

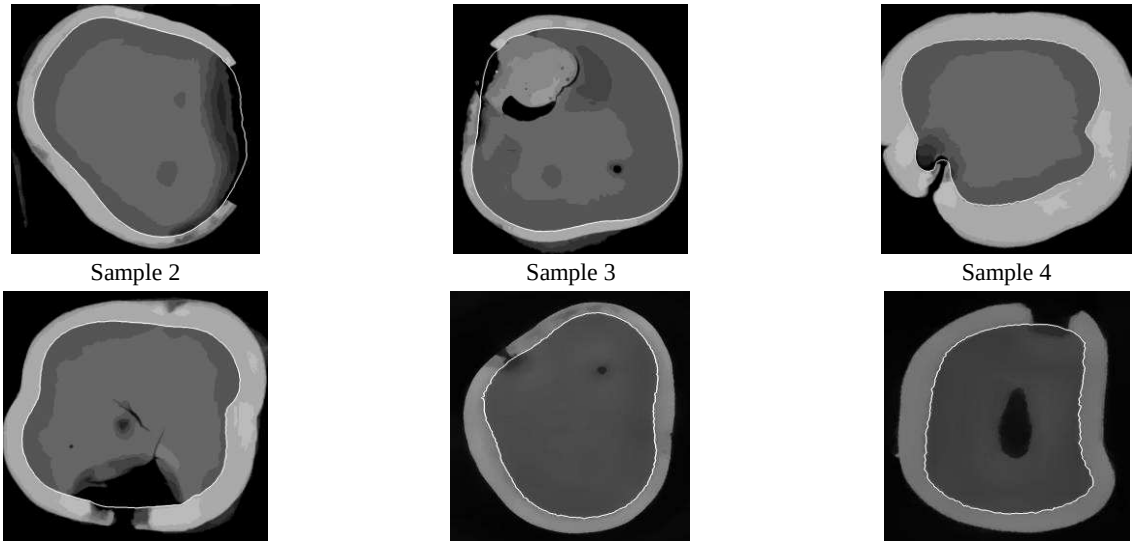

Sample 2 Sample 3 Sample 4

Sample 5 Sample 6 Sample 7

Fig. 16. Selected horizontal slices of the final results of the estimation process from six image datasets, showing the accurate estimation of the destructed DEJ contour and precise tracking of the DEJ interface in sound areas.

Table I. Overall comparative results of the quantitative evaluation of the contour-based (MD, HD, RDE) and area-based metrics (OR, UR, ER) for seven image datasets. T1 and T2 indicate the standard results manually traced by two experts and T1T2 indicates the average of T1 and T2.

	MD (μm)	**HD (μm)**	**RDE (μm)**	**OR (%)**	**UR (%)**	**ER (%)**
T1 vs. T2	7.3389±0.2714	43.8787±55.7415	10.8250±0.9576	0. 29±~0	0. 35±~0	0. 64±~0
Proposed method vs. T1	14.450±2.1849	98.5025±195.8329	23.1622±14.0646	0. 55±~0	0. 76±~0	1.22±~0
Proposed method vs. T2	14.490±2.2962	99.7698±196.5565	23.2850±5.0970	0. 52±~0	0. 79±~0	1.22±~0
Proposed method vs. T1T2	14.879±3.8732	98.7455±193.6435	23.5930±6.7773	0. 51±~0	0. 84±~0	1.25±~0

A. Visual results

Figure 14 shows the 3D visualization result of the application of the proposed method on a stack of 250 images from a nominated image dataset, where green color indicates sound DEJ interface and the red indicates reconstructed DEJ. The results of the reconstruction process in several horizontal slices from the same dataset are also shown in Figure 15 to provide a better verification of the retrieval performance of the method. Figure 16 shows selected horizontal slices of the estimation results from six more image datasets.

B. Quantitative evaluation

The quantitative evaluation of the performance of the proposed method was implemented using several contour and area-based metrics. To calculate these metrics, 10 slices were chosen randomly from each of the seven image datasets and the overall result was calculated by averaging the obtained parameter values for all datasets.

Contour-based evaluation metrics, which included Mean Distance (MD), Hausdorff Distance (HD) [32] and Relative Distance Error (RDE) [33], were calculated by comparing the estimated contour by the algorithm with the standard results manually traced by two experts (T1 and T2) and the resultant average of T1 and T2 (T1T2). The MD and HD describe the average and maximum point-to-point Euclidian distance between estimated and manual contours respectively. $\boldsymbol{A} = \{\boldsymbol{a_1}, \dots, \boldsymbol{a_p}\}$ and $\boldsymbol{M} = \{\boldsymbol{m_1}, \dots, \boldsymbol{m_q}\}$ represent the resultant contour of the proposed method and manual tracing respectively. The distance between the point $\boldsymbol{a_i} \in \boldsymbol{A}$ and the contour $\boldsymbol{M}$ is defined as

$$\boldsymbol{D(a_i, M) = \min_j \|m_j - a_i\|} \quad (18)$$

Mean Distance (MD) and Hausdorff Distance (HD) are defined as

$$\boldsymbol{MD(A, M) = mean_i\left(mean_j\left(D(a_i, M)\right), mean_j\left(D(m_j, A)\right)\right)} \quad (19)$$

$$\boldsymbol{HD(A, M) = max_i\left(max_j\left(D(a_i, M)\right), max_j\left(D(m_j, A)\right)\right)} \quad (20)$$

RDE represents the difference of contours between the extracted boundary and the manual tracing:

$$\boldsymbol{RDE = \frac{1}{2}\left(\sqrt{\frac{1}{p}\sum_{i=1}^{p} d_{a_i}^2} + \sqrt{\frac{1}{q}\sum_{j=1}^{q} d_{m_j}^2}\right)} \quad (21)$$

where

$$\boldsymbol{d_{a_j}^2 = \min\{distance(a_i, m_j) | j = 1, \dots, q\}}$$
$$\boldsymbol{d_{m_i}^2 = \min\{distance(m_j, a_i) | i = 1, \dots, p\}}$$

The overall results of the contour based evaluation metrics for all image datasets (Table I) indicate that regarding MD, the average of distance error between the estimated contour by the proposed method and the results from manual tracing (T1T2) (14.87 μm equivalent to ~2 pixels) are close to the value of the error between the two human experts, i.e. T1 and T2 (7.33 μm). The overall results of HD metric show that the average of maximum distance error between the proposed method and T1T2 is close to the value of the error between T1 and T2. Moreover, RDE, which calculates the standard deviation of distance error, had a low average value of 23.5930 μm (less than three pixels).

Area-based evaluation metrics included three common error measures namely, Over-segmentation Rate (OR), Under-segmentation Rate (UR) and overall Error Rate (ER).

$$\boldsymbol{OR = Q_p/(U_p + D_p)} \quad (22)$$
$$\boldsymbol{UR = U_p/(U_p + D_p)} \quad (23)$$
$$\boldsymbol{ER = (Q_p + U_p)/D_p} \quad (24)$$

Here, $\boldsymbol{Q_p}$ indicates the number of pixels that should be included in the segmentation results but are not included, $\boldsymbol{U_p}$ is the number of pixels that should not be included in the segmentation results but are included, and $\boldsymbol{D_p}$ is the number of pixels which are included in the segmentation results correctly [33]. The results of the area based metrics evaluation (Table I) indicated that there is about 1% difference in the OR, UR and ER values of the proposed method with the corresponding values from T1, T2 and T1T2. This level of difference between the machine-based method and manual methods was comparable to the difference between two experts (T1 and T2).

V. Discussion

In this paper, we proposed a novel sequential approach for estimating the contour of a missing surface using modified TRM. First, the initial edge information is determined automatically or manually, for the starting slice. The extracted information from this contour defines the local search area and provides the overall estimation pattern for the edge candidates in the next slice. The search for edge candidates in the following slice is performed in the perpendicular direction to the obtained initial edge in order to find and label the corrupted edge candidates. Subsequently, the location information of both the initial and the nominated edge candidates is transformed into two independent signals (X-coordinates and Y-coordinates) and the problem is changed to error concealment. In the next step, the missing samples of these signals, corresponding to the labeled edge candidates, are estimated using the proposed modified TRM model and finally, the reconstructed signals are transformed inversely to edge pixel representation. The estimated edges in each slice are considered as initial edge information for the next slice and this procedure is repeated slice by slice until the entire contour of the destructed surface is estimated.

The performance and accuracy of the proposed method in comparison to the manual results by two human experts, evaluated by contour-based and area-based metrics, proved to be satisfactory for the assessed cases. For example, the average of distance error between the estimated contour by the proposed method and the contour from manual tracing (14.87 μm) is comparable to that between the two human experts (7.33 μm). Although the numerical value of the error is nearly twice the error by the human experts, however, considering the thickness of the specimen (in the case of dental enamel having an average thickness of 1500 μm), the amount of the error lays within the acceptable range.

The distribution of six quantitative metrics including contour-based (MD, HD, RDE) and area-based (OR, UR, ER) metrics for 70 nominated image slices from seven specimens are shown in Figures 17.a and 17.b. In these two charts, every 10 successive samples belong to one specimen and the slices were selected from the beginning, center and the end of each

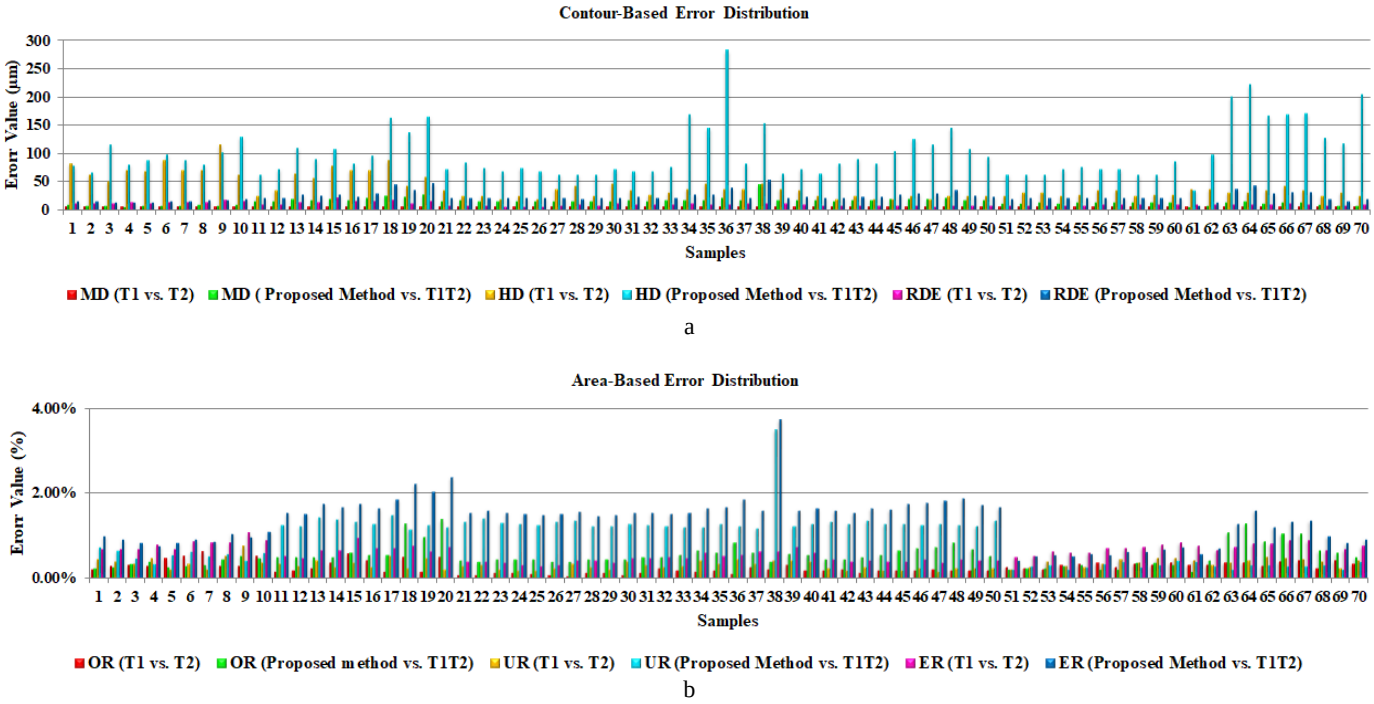

Fig. 17. Error distribution charts for the contour-based (MD, HD, RDE) and area-based (OR, UR, ER) metrics for 70 nominated image slices from seven specimens. Every 10 successive samples in the charts belong to one specimen.

destructed surface. As shown in Figure 17, the error value depends on the amount of surface destruction and the level of corresponding signal corruption. Accordingly, the error values are highest for the slices from highly destructed regions, especially for the slices selected from the middle of the destructed area.

An important aspect of the proposed mathematical model was the addition of two similarity terms to the original regularization model. Here we discuss the addition of these terms by evaluating the effect of each added term on the retrieved signal and the resultant reconstructed DEJ contour.

First, we consider Eq. (13), without the addition of the similarity terms. Figures 18.a to 18.c show the result of the application of the original TRM on the destructed image before adding the two similarity terms. In each row of Figure 18 and later in Figure 19, the columns on the left, center and right side illustrate $\boldsymbol{C_x}$, $\boldsymbol{C_y}$ and corresponding pixel representation of $\boldsymbol{C_x}$ and $\boldsymbol{C_y}$ on the image, respectively. As mentioned in Section III.C, because of the gradual loss of intensity in the marginal regions around the lesion (red circles in Figure 2.b), some mildly corrupted edge candidates are also detected inadvertently as sound DEJ (red circles in Figure 18.a right). Although with the denoising effect of $\|\boldsymbol{\beta D''e}\|_2^2$ (for normal value of $\boldsymbol{\beta}$), small distortions are removed, but for this group of marginal samples, the distortion is not eliminated satisfactorily and the samples are not properly smoothed. Figure 18.b shows the pure smoothing function of $\|\boldsymbol{\beta D''e}\|_2^2$ (apart from its estimation function) in which the estimated samples from the reconstructed $\boldsymbol{C_x}$ and $\boldsymbol{C_y}$ signals have been eliminated and only the existing samples smoothed by $\|\boldsymbol{\beta D''e}\|_2^2$ are left. The improper smoothing of the samples shown in Figure 18.b has led to severe distortion of marginal samples and incorrect estimation of the missing samples and the resultant edge points (Figure 18.c).

A potential way for decreasing the distortion of marginal samples is by increasing the effect of $\|\boldsymbol{\beta D''e}\|_2^2$. However, this increase will change the curved shape of the signals to a straight line in the marginal region. Therefore, to overcome the problem of distortion in the marginal samples, we added $\|\boldsymbol{\gamma S_s(e-z)}\|_2^2$ to the regular TRM. The effect of adding $\|\boldsymbol{\gamma S_s(e-z)}\|_2^2$ to the original TRM can be observed by comparing the corrupted signal in Figure 18.d with Figure 18.a. The function of $\|\boldsymbol{\gamma S_s(e-z)}\|_2^2$, which is localized to the marginal samples, is to decrease the distortion by forcing the marginal samples to follow the trend of the corresponding samples of the signals from the previous slice. It must be noted that $\|\boldsymbol{\gamma S_s(e-z)}\|_2^2$ and $\|\boldsymbol{\alpha S(e-c)}\|_2^2$ have similar functions but opposite objectives. The goal of $\|\boldsymbol{\alpha S(e-c)}\|_2^2$ is to preserve the existing value of the known samples (which include undesirable mildly corrupted marginal samples) in the final resultant signal. On the other hand, the goal of $\|\boldsymbol{\gamma S_s(e-z)}\|_2^2$ is to modify the value of marginal samples by incorporating the value of the corresponding samples from the previous slice. Accordingly, to increase the effect of $\|\boldsymbol{\gamma S_s(e-z)}\|_2^2$ more than $\|\boldsymbol{\alpha S(e-c)}\|_2^2$, the coefficients of $\|\boldsymbol{\gamma S_s(e-z)}\|_2^2$ must be tuned in a way that for the marginal samples $\boldsymbol{\gamma > \alpha}$. In fact, $\|\boldsymbol{\gamma S_s(e-z)}\|_2^2$ applies an extra denoising model alongside the denoising role of $\|\boldsymbol{\beta D''e}\|_2^2$, on the marginal samples. The result of denoising and estimation after adding $\|\boldsymbol{\gamma S_s(e-z)}\|_2^2$ to the original TRM are shown in Figures 18.e and 18.f respectively.

Until now, the proposed objective function has evolved to $\|\boldsymbol{\alpha S(e-c)}\|_2^2 + \|\boldsymbol{\beta D''e}\|_2^2 + \|\boldsymbol{\gamma S_s(e-z)}\|_2^2$ in which, only $\|\boldsymbol{\beta D''e}\|_2^2$ contributes to the estimation of missing samples located at the central region of the corrupted signal (a group of $\boldsymbol{N_g}$ samples). As mentioned earlier, $\|\boldsymbol{\beta D''e}\|_2^2$ contributes in the estimation process by enforcing the missing samples to follow the trend and the curve shape of the known samples of the signal. Accordingly, based on the direction of the existing samples

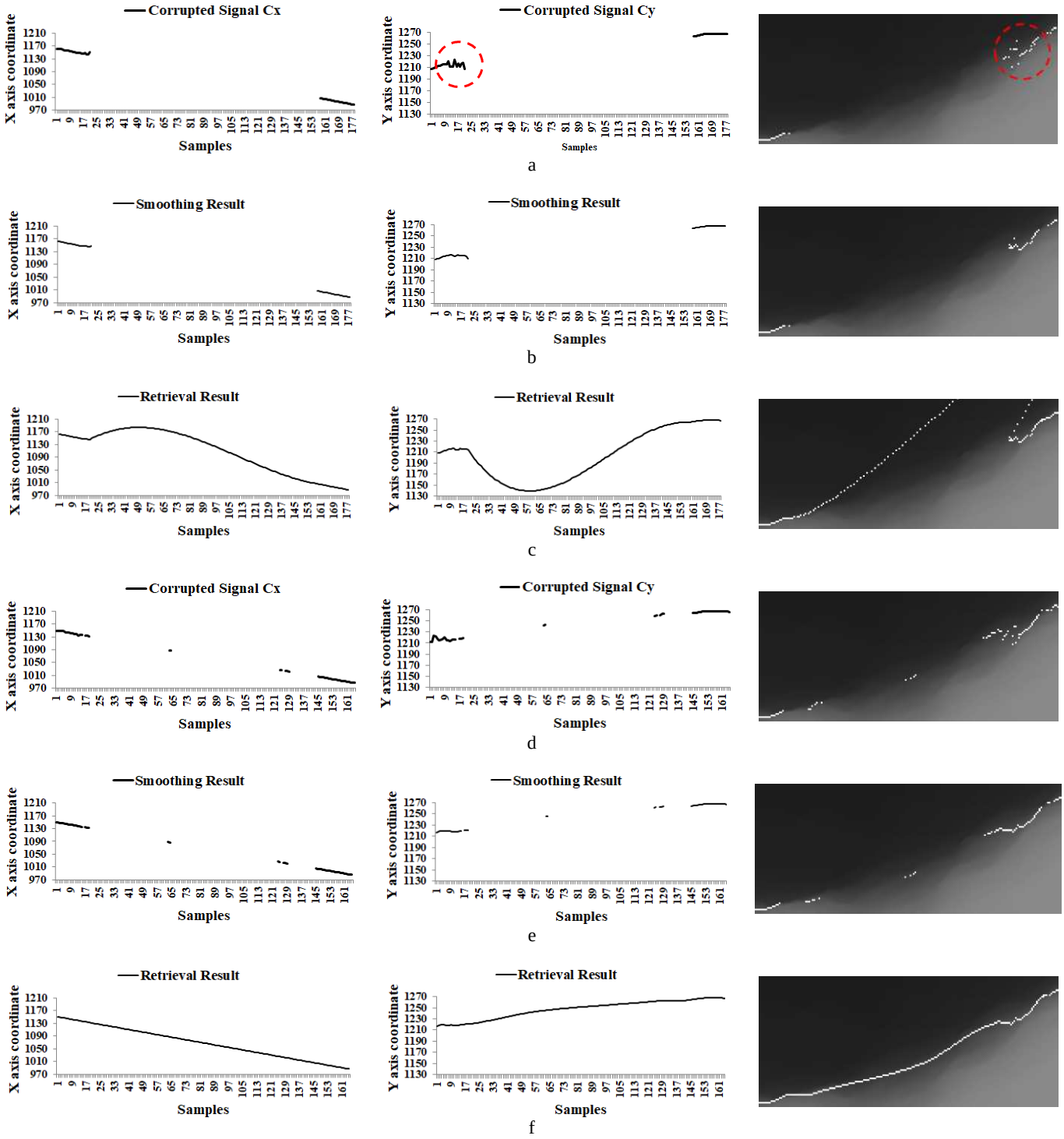

Fig. 18. Effect of adding $\|\gamma \boldsymbol{S}_s(\boldsymbol{e}-\boldsymbol{z})\|_2^2$ to regular TRM. Left column shows $\boldsymbol{c}_x$, middle column shows $\boldsymbol{c}_y$ and right column shows embedded results on the image. a) Corrupted signals of edge candidates before adding $\|\gamma \boldsymbol{S}_s(\boldsymbol{e}-\boldsymbol{z})\|_2^2$, b) Smoothing results for edge candidates before adding $\|\gamma \boldsymbol{S}_s(\boldsymbol{e}-\boldsymbol{z})\|_2^2$ to the original TRM**,** c) Retrieval results for edge candidates before adding $\|\gamma \boldsymbol{S}_s(\boldsymbol{e}-\boldsymbol{z})\|_2^2$, d) Corrupted signals for edge candidates after adding $\|\gamma \boldsymbol{S}_s(\boldsymbol{e}-\boldsymbol{z})\|_2^2$, e) Smoothing results for edge candidates after adding $\|\gamma \boldsymbol{S}_s(\boldsymbol{e}-\boldsymbol{z})\|_2^2$ **,** f) Retrieval results for edge candidates before adding $\|\gamma \boldsymbol{S}_s(\boldsymbol{e}-\boldsymbol{z})\|_2^2$. In figures a, b, d and e the estimated samples from the reconstructed $\boldsymbol{c}_x$ and $\boldsymbol{c}_y$ signals have been eliminated and only the existing samples smoothed by $\|\boldsymbol{\beta D}''\boldsymbol{e}\|_2^2$ are left.

located at two sides of the corrupted region (samples 73 and 205 in Figure 19.b center), 2nd-order curves are estimated without any control (Figure 19.c center) which adversely affect the estimation results (Figure 19.c right). By adding $\|\boldsymbol{\zeta S}_s\boldsymbol{D}'(\boldsymbol{e}-\boldsymbol{z})\|_2^2$ alongside $\|\boldsymbol{\beta D}''\boldsymbol{e}\|_2^2$, we enforced the estimation of the missing samples located at the center of the corrupted signal, to achieve the highest similarity to the shape of the corresponding samples from the DEJ of the previous slice. Figures 19.d, 19.e and 19.f show the corrupted signal, smoothing result and retrieving result for the missing samples alongside the related images after the addition of $\|\boldsymbol{\zeta S}_s\boldsymbol{D}'(\boldsymbol{e}-\boldsymbol{z})\|_2^2$ to $\|\boldsymbol{\alpha S}(\boldsymbol{e}-\boldsymbol{c})\|_2^2+\|\boldsymbol{\beta D}''\boldsymbol{e}\|_2^2+\|\gamma \boldsymbol{S}_s(\boldsymbol{e}-\boldsymbol{z})\|_2^2$.

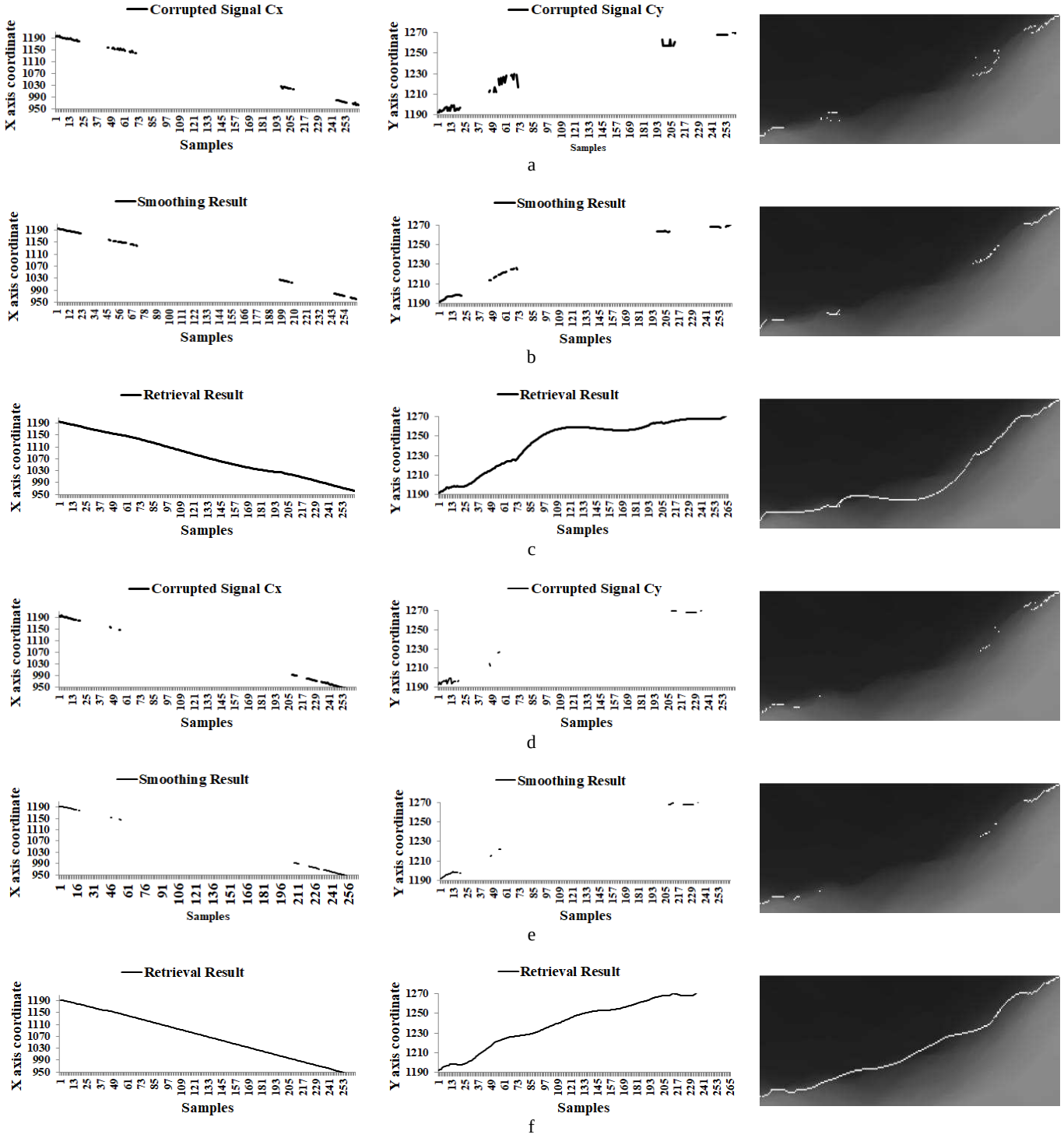

Fig. 19. Effect of adding $\|\zeta S_s D'(e-z)\|_2^2$ to regular TRM after the addition of $\|\zeta S_s D'(e-z)\|_2^2$. Left column shows C_x, , central column shows C_y and the right column shows the embedded results on the image. a) Corrupted signals of edge candidates before adding $\|\zeta S_s D'(e-z)\|_2^2$, b) Smoothing results for edge candidates before adding $\|\zeta S_s D'(e-z)\|_2^2$, c) Retrieval results for edge candidates before adding $\|\zeta S_s D'(e-z)\|_2^2$, d) Corrupted signals for edge candidates after adding $\|\zeta S_s D'(e-z)\|_2^2$, e) Smoothing results for edge candidates after adding $\|\zeta S_s D'(e-z)\|_2^2$, f) Retrieval results for edge candidates after adding $\|\zeta S_s D'(e-z)\|_2^2$.

Regarding the application of the developed method, it is worth mentioning that the two main parts of the proposed method (segregation and transformation of the location information of edge pixels into two 1D corrupted signals and estimation of the missing samples of the corrupted signals and corresponding destructed surface) are independent of the type of the image and the application. Accordingly, this method may find application for reconstructing the destructed contour of biological tissues, valuable historical and rare objects, or any 3D structure with reasonable level of complexity and damage. The proposed method was also tested on three other different datasets including a destructed human skull, damaged mandibular and zygomatic bones, and a vein with missing media adventitia boundary [34]. The estimation results for these datasets, showed the satisfactory performance of the method for non-dental datasets (Figure 20).

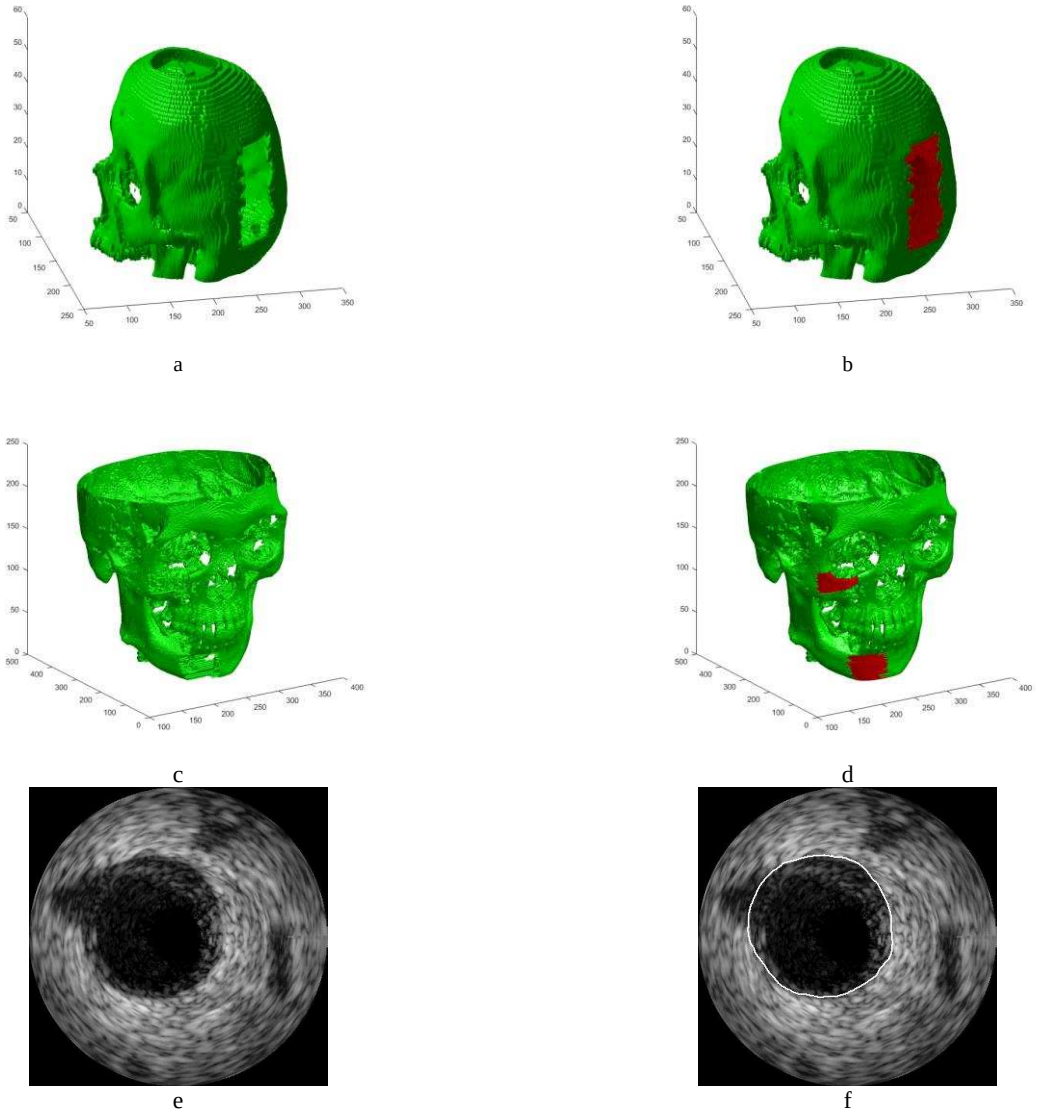

Fig. 20. Visualization of the destructed surface and final results of estimation in three datasets. a,b) Skull c,d) zygomatic and mandibular bones. e,f) media adventitia boundary.

It should be noted that the proposed method has limitations in estimating the contour of structures with very complex and highly variable patterns in which the changes in the contour between consecutive slices, takes place rapidly and not in a gradual manner.

Finally, it is worth mentioning that besides the capabilities of the proposed method for accurate estimation of the shape and position of a destructed surface in three dimensions, it has the advantage of simultaneous estimation of multiple destructed contours with different orders. This capability can be observed in Figure 15, where the estimated contour of the lower lesion (corresponding to the region D2 in Figure 2.b) changes from 2^{nd}- to 3^{rd}-order gradually while the upper lesion (corresponding to the region D1 in Figure 2.b) is estimated by a 2^{nd}-order contour at the same time.

VI. Conclusion

This study proposed a sequential method for the estimation and reconstruction of the pre-existing contour of a damaged 3D surface. The method was motivated by a one-dimensional signal processing technique called error concealment in which the missing samples of a signal are retrieved based on the information from the existing sound samples. A major advantage of the proposed method is the convenient yet accurate retrieval of the missing data through the transformation of the 3D problem into a 1D problem, and by proposing a simple convex model. The visual results (Figures 14, 15, 16 and 20) as well as contour-based and area-based quantitative evaluation (Table I), showed that the utilized TRM-based error concealment method can accurately interpolate the shape and the position of the destructed contour in both two and three dimensions.

Acknowledgement

The authors would like to thank Ms. Gina Browne, Dr. Aline de Almeida Neves, Dr. Hui Li, Dr. Simone Balocco and the Australian Center for Microscopy and Microanalysis.

REFERENCES

[1] H. N. Chia and B. M. Wu, "Recent advances in 3D printing of biomaterials," Journal of biological engineering, vol. 9, p. 1, 2015.

[2] W. Wu, Y. Zhang, H. Li, and W. Wang, "Fabrication of repairing skull bone defects based on the rapid prototyping," Journal of Bioactive and Compatible Polymers, vol. 24, pp. 125-136, 2009.

[3] A. L. Bertozzi, S. Esedoglu, and A. Gillette, "Inpainting of binary images using the Cahn-Hilliard equation," IEEE Transactions on image processing, vol. 16, pp. 285-291, 2007.

[4] Y. Li, D. Jeong, J.-i. Choi, S. Lee, and J. Kim, "Fast local image inpainting based on the Allen–Cahn model," Digital Signal Processing, vol. 37, pp. 65-74, 2015.

[5] J. Bosch and M. Stoll, "A Fractional Inpainting Model Based on the Vector-Valued Cahn--Hilliard Equation," SIAM Journal on Imaging Sciences, vol. 8, pp. 2352-2382, 2015.

[6] J. Bosch, D. Kay, M. Stoll, and A. J. Wathen, "Fast solvers for Cahn--Hilliard inpainting," SIAM Journal on Imaging Sciences, vol. 7, pp. 67-97, 2014.

[7] C.-b. Schönlieb and A. Bertozzi, "Unconditionally stable schemes for higher order inpainting," Commun. Math. Sci, vol. 9, pp. 413-457, 2011.

[8] M. Burger, L. He, and C.-B. Schönlieb, "Cahn-Hilliard inpainting and a generalization for grayvalue images," SIAM Journal on Imaging Sciences, vol. 2, pp. 1129-1167, 2009.

[9] J. A. Dobrosotskaya and A. L. Bertozzi, "A wavelet-Laplace variational technique for image deconvolution and inpainting," IEEE Transactions on Image Processing, vol. 17, pp. 657-663, 2008.

[10] F. Y. Shih and S. Cheng, "Adaptive mathematical morphology for edge linking," Information sciences, vol. 167, pp. 9-21, 2004.

[11] A. D. Sappa and B. X. Vintimilla, "Edge point linking by means of global and local schemes," in Signal Processing for Image Enhancement and Multimedia Processing, ed: Springer, 2008, pp. 115-125.

[12] A. Jevtić, I. Melgar, and D. Andina, "Ant based edge linking algorithm," in Industrial Electronics, 2009. IECON'09. 35th Annual Conference of IEEE, 2009, pp. 3353-3358.

[13] R. Priyakanth and M. B. Sankar, "A NOVEL METHOD FOR EDGE DRAWING OR LINKING USING SOBEL GRADIENT," International Journal of Engineering Science and Technology, vol. 4, 2012.

[14] F. Li, S. Gao, W. Wang, and Z. Tang, "An adaptive clonal selection algorithm for edge linking problem," IJCSNS International Journal of Computer Science and Network Security, vol. 9, pp. 57-65, 2009.

[15] S.-M. Liu, W.-C. Lin, and C.-C. Liang, "An iterative edge linking algorithm with noise removal capability," in Pattern Recognition, 1988., 9th International Conference on, 1988, pp. 1120-1122.

[16] M. Xie, "Edge linking by using causal neighborhood window," Pattern recognition letters, vol. 13, pp. 647-656, 1992.

[17] F. L. Miller, J. Maeda, and H. Kubo, "Template based method of edge linking using a weighted decision," in Intelligent Robots and Systems' 93, IROS'93. Proceedings of the 1993 IEEE/RSJ International Conference on, 1993, pp. 1808-1815.

[18] J. Li, J. Randall, and L. Guan, "Perceptual image processing for digital edge linking," in Electrical and Computer Engineering, 2003. IEEE CCECE 2003. Canadian Conference on, 2003, pp. 1215-1218.

[19] H. Kimm, N. Abolhassani, and F. Lee, "Edge Detection and Linking Pattern Analysis Using Markov Chains," in Computational Science and Engineering (CSE), 2013 IEEE 16th International Conference on, 2013, pp. 1146-1152.

[20] B. Dong, A. Chien, Z. Shen, and S. Osher, "A new multiscale representation for shapes and its application to blood vessel recovery," SIAM Journal on Scientific Computing, vol. 32, pp. 1724-1739, 2010.

[21] B. Dong, Q. Jiang, C. Liu, and Z. Shen, "Multiscale representation of surfaces by tight wavelet frames with applications to denoising," Applied and Computational Harmonic Analysis, vol. 41, pp. 561-589, 2016.

[22] A. Schmieder, "Cell Path Reconstruction Using 3D Digital Inpainting," Ms thesis, University of Waterloo, 2013.

[23] Y. Wang and Q.-F. Zhu, "Error control and concealment for video communication: A review," Proceedings of the IEEE, vol. 86, pp. 974-997, 1998.

[24] M. Lashgari, H. Rabbani, M. Shahmorad, and M. Swain, "A fast and accurate dental micro-CT image denoising based on total variation modeling," in Signal Processing Systems (SiPS), 2015 IEEE Workshop on, 2015, pp. 1-5.

[25] M. Shahmoradi, M. Lashgari, H. Rabbani, J. Qin, and M. Swain, "A comparative study of new and current methods for dental micro-CT image de-noising," Dentomaxillofacial Radiology, p. 20150302, 2016.

[26] I. Selesnick, "Least squares with examples in signal processing," Connexions, April 2013.

[27] R. Ramlau, "Regularization properties of Tikhonov regularization with sparsity constraints," Electron. Trans. Numer. Anal, vol. 30, pp. 54-74, 2008.

[28] C. E. Smith and H. Schaub, "Efficient polygonal intersection determination with applications to robotics and vision," in Intelligent Robots and Systems, 2005.(IROS 2005). 2005 IEEE/RSJ International Conference on, 2005, pp. 3890-3895.

[29] A. Oliveira, S. Ribeiro, R. Farias, and C. Esperanca, "Loop snakes: Snakes with enhanced topology control," in Computer Graphics and Image Processing, 2004. Proceedings. 17th Brazilian Symposium on, 2004, pp. 364-371.

[30] L. Ji and H. Yan, "Loop-free snakes for highly irregular object shapes," Pattern recognition letters, vol. 23, pp. 579-591, 2002.

[31] A. Nakhmani and A. Tannenbaum, "Self-crossing detection and location for parametric active contours," Image Processing, IEEE Transactions on, vol. 21, pp. 3150-3156, 2012.

[32] A. Vard, K. Jamshidi, and N. Movahhedinia, "An automated approach for segmentation of intravascular ultrasound images based on parametric active contour models," Australasian physical & engineering sciences in medicine, vol. 35, pp. 135-150, 2012.

[33] C. Pan, D. S. Park, S. Yoon, and J. C. Yang, "Leukocyte image segmentation using simulated visual attention," Expert Systems with Applications, vol. 39, pp. 7479-7494, 2012.

[34] S. Balocco, C. Gatta, F. Ciompi, A. Wahle, P. Radeva, S. Carlier, et al., "Standardized evaluation methodology and reference database for evaluating IVUS image segmentation," Computerized Medical Imaging and Graphics, vol. 38, pp. 70-90, 2014.